

# We are IntechOpen, the world's leading publisher of Open Access books Built by scientists, for scientists

6,000

Open access books available

148,000

International authors and editors

185M

Downloads

Our authors are among the

154

Countries delivered to

TOP 1%

most cited scientists

12.2%

Contributors from top 500 universities



WEB OF SCIENCE™

Selection of our books indexed in the Book Citation Index  
in Web of Science™ Core Collection (BKCI)

Interested in publishing with us?  
Contact [book.department@intechopen.com](mailto:book.department@intechopen.com)

Numbers displayed above are based on latest data collected.  
For more information visit [www.intechopen.com](http://www.intechopen.com)



# Digital Holographic Microscopy in Partially Coherent Illumination and Applications

*Frank Dubois, Catherine Yourassowsky,  
Karim Zouaoui Boudjeltia and Jérôme Dohet-Eraly*

## Abstract

In this chapter, we describe several configurations of digital holographic microscopes operating with partially coherent illumination, including the implementation of color holography. The different ways of implementing partially coherent illumination are described and discussed, as well as the respective improvements they provide depending on the properties of the observed objects. Several significant applications in the biomedical and environmental fields are presented. In particular, we carry out researches on correlative quantitative phase-contrast-fluorescence imaging on blood with a special focus on the behavior of platelets in relation to relevant pathologies. In the environmental domain, we demonstrate the use of high-throughput digital holographic microscopy to monitor and analyze plankton and microalgal cultures.

**Keywords:** digital holographic microscopy, partially coherent illumination, coherent noise reduction, quantitative phase-contrast imaging, digital refocusing, environmental applications, biomedical applications

## 1. Introduction

Classical optical microscopy is highly limited by the small depth of focus due to the high magnification coupled with the high numerical apertures. With such a constraint, the analysis of a three-dimensional (3D) sample is complex and even impossible in the case of dynamic phenomena, which makes the extension of the depth of focus an important challenge. With the impressive recent developments of digital cameras, digital holography has provided an elegant and natural tool to counteract this limitation by enabling numerical refocusing at different depths within an experimental volume [1, 2]. In this context, digital holographic microscopy (DHM), which drastically increases the depth of focus (about  $100\times$ ), became a very powerful tool to investigate numerous applications, in particular in the biomedical and environmental fields. Moreover, thanks to the wave nature of holography, DHM may provide the quantitative phase-contrast imaging (QPCI) that considerably extends the potential of this technology, especially in biological and environmental applications [3–6]. Several ways exist to implement DHM. The conceptually simplest implementation consists of

using an interferometric configuration: it allows to record the interference pattern between the object beam, resulting from the transmission through—or the reflection by—the object, and a separated reference beam [2, 7, 8]. Hereinafter, those configurations are called two-channel interferometers. Several other ways to proceed may be considered. Firstly, common-path interferometers [5, 9] allow to simplify the configuration or to improve mechanical robustness. However, other limitations may arise from the common-path configurations as, in some cases, the apparition of halo effects in the phase images or the difficulties to implement an illumination of partial coherence. Other configurations were also developed that aim to reach the same goals as, for instance, the implementation of the transport of the intensity equation in a usual microscope [10], the in-line holography [11] and the ptychography [12]. Those configurations are interesting but request more complex computations to get the results, which can make reconstruction ability or the quantitative phase recovery more difficult. However, with two-paths interferometers, the full complex amplitude, required for the refocusing process and the QPCI, is obtained with relatively simple and straightforward computation. Regarding the mechanical robustness of the two-channel configuration, our experience has shown that it is not actually an issue. The design of the compact optical system with usual optomechanical components indeed allows to build systems that are able to operate even in the harsh environment [13–15].

The most usual way to implement holography in a two-channel configuration is to use a laser source; it is then easy to have mutually coherent object and reference beams, giving interference patterns on the camera. However, coherent beams are very sensitive to any disturbance in their propagation, which leads to noisy results. This noise that alters the images, which is related to the speckle effect, is multiplicative and hence difficult to remove by post-processing. Additionally, the speckle disturbance is created everywhere in the optical setup and experimental cells from any small defect. For this reason, we developed several DHM configurations taking advantage of partially coherent illuminations. The use of such illuminations drastically reduces the noise in both the amplitude modulus and phase images.

It has to be noted that a lot of researches were also performed to develop digital holography to get holographic information with completely incoherent light, and in particular from fluorescent objects. Pioneer articles in this field are given by the references [16–18].

In Section 2, we present the DHM configurations, developed with partially coherent illumination, and the processing to obtain the amplitude modulus and the phase from the recorded hologram. Section 2 also describes how the fluorescence can be implemented to achieve multimodal DHM (see details in Section 4.1) and the extension of the technology to color DHM with partially coherent illumination. The benefit of using partially coherent illumination to drastically reduce the speckle noise is demonstrated in Section 3. In Section 4, we describe several valuable applications we implemented.

## **2. DHM configurations with partially coherent sources**

When implemented in a DHM configuration, it is requested that the partial spatial coherence of the beam illuminating the sample is uniform over the complete field of view. Therefore, the mutual coherence function  $\Gamma$  has to be expressed, in a plane, as a function ( $\gamma$ ) of the difference between the considered positions  $\mathbf{x}_1 = (x_1, y_1)$  and  $\mathbf{x}_2 = (x_2, y_2)$ :

$$\Gamma(\mathbf{x}_1, \mathbf{x}_2) = \gamma(\mathbf{x}_1 - \mathbf{x}_2) \quad (1)$$

Such a mutual coherence function can be obtained from a spatially incoherent source or from a spatially highly coherent source according to the schemes in **Figure 1** [19].

On the left configuration in **Figure 1**, a fully spatially incoherent beam is illuminating an aperture  $p(\mathbf{x})$ . The aperture is placed at the front focal plane of a collimation lens. Assuming we have a quasi-monochromatic illumination, it results out of the lens a partial spatial coherence function that can be expressed by:

$$\gamma(\mathbf{x}_1 - \mathbf{x}_2) \propto (Fp)((\mathbf{x}_1 - \mathbf{x}_2)/\lambda f) \quad (2)$$

where  $F$  denotes the two-dimensional Fourier transformation,  $f$  is the focal length of the lens, and  $\lambda$  is the wavelength. The left configuration of **Figure 1** also allows the implementation of sources of reduced temporal coherence like light-emitting diodes (LEDs). However, the aperture removes a large part of the source intensity and the use of LEDs is more complex if the interferometric off-axis configuration is used.

It is also possible to obtain an equivalent partial spatial coherence illumination by the right configuration in **Figure 1**, in which a laser source is focused close to a rapidly moving ground glass placed at the front focal plane of a collimating lens. The ground glass generates a speckle field, whose width is adjusted by changing the position of the focused laser beam with respect to this ground glass and by the choice of the focal length of the collimating lens. It can be observed that, with time averaging, this source can be seen as a partially spatially coherent source, whose typical coherence width is equal to the average speckle size [20].

In the following, we describe two particular implementations of DHM with partially coherent illumination that we developed. The first one uses monochromatic illumination and can be coupled with a fluorescence module to achieve a multimodal instrument. It is shown in **Figure 2a**. A coherent beam emerging from a mono-mode laser diode is focalized by the lens ML1 close to the rough surface of the rotating ground glass (GG). The light transmitted by the GG is scattered and collimated by the lens L1. A first beam splitter BS1 divides the collimated beam into an object beam and a reference beam. The object beam passes through the sample and then through the microscope lens ML3. In a symmetric way, the reference beam passes through the microscope lens ML2, identical to ML3. Reference and object beams are then recombined by a second beam splitter (BS2) and transmitted by lens L2. Lenses ML3–L2 image one plane of the sample onto the camera sensor. The magnification  $G_s$  is then given by the ratio between the focal length of L2 and the focal length of ML3. Depending on the applications, the magnification is adjusted by changing the

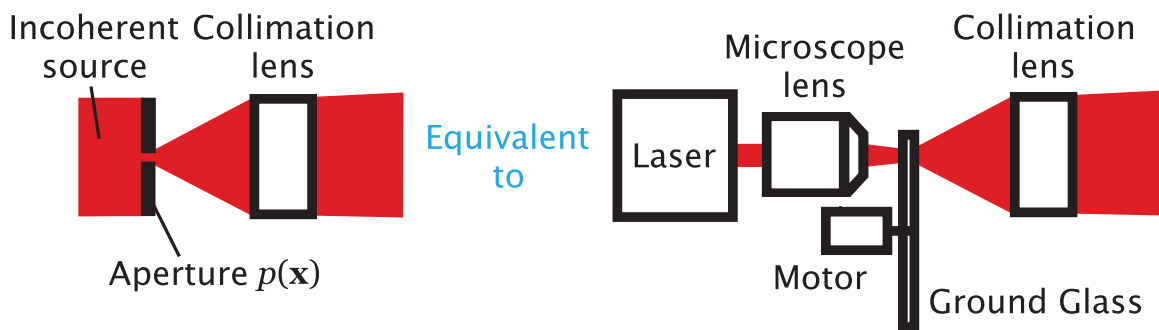


**Figure 1.**  
 Two ways to obtain a spatially partial mutual coherence function.

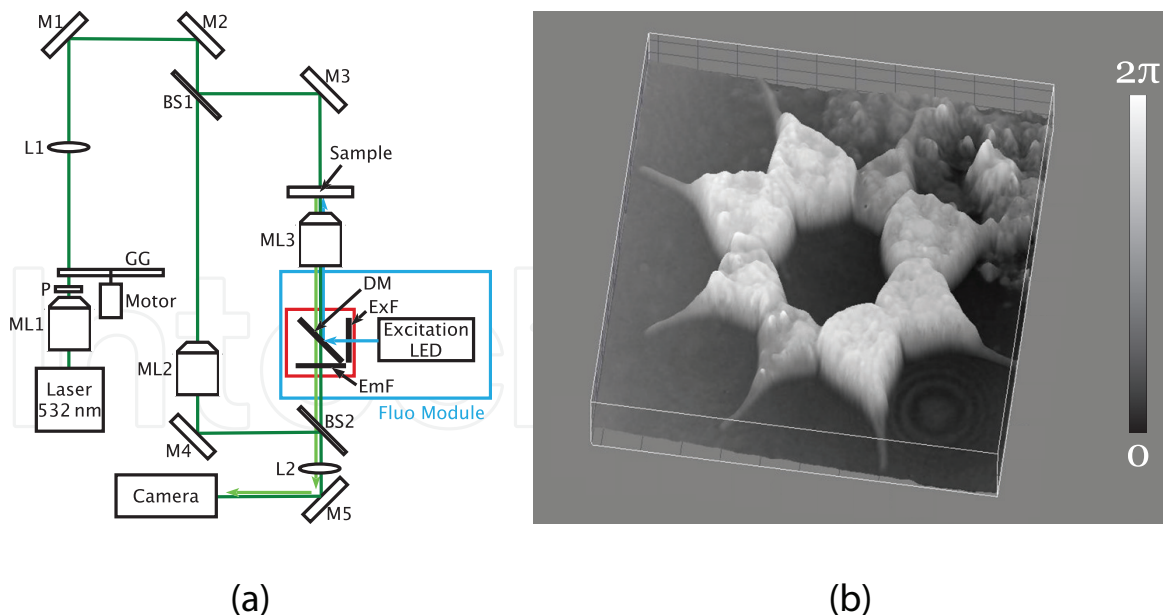


**Figure 2.** Monochromatic DHM coupled with fluorescence to achieve a multimodal instrument. (a) diagram of the instrument. ML1-ML3: microscope lenses, P: polarizer, GG: ground glass, L1-L2: lenses, BS1-BS2: beam splitters, M1-M5: mirrors, EmF: emission filter, ExF: excitation filter, and DM: dichroic mirror. (b) 3D plot of the quantitative phase-contrast image of an alga *Pediastrum* sp. Field of view:  $80 \times 80 \mu\text{m}$ , magnification  $\times 100$ , NA: 1.3-oil immersion lens.

couple of lenses ML2 and ML3 (typically we used microscope lenses  $\times 10$ ,  $\times 20$ ,  $\times 40$ ,  $\times 63$ , and  $\times 100$  (immersion oil)).

In most of the applications, the interferometer is adjusted to have a slanted reference beam with respect to the object beam in such a way that a thin fringe pattern is recorded on the camera sensor. The computation of the full complex amplitude from every recorded hologram, involving the amplitude modulus and the phase, is obtained by using the Fourier method [21]. In the resulting phases, it happens that unwanted phase modulations appear, which can be originated from the experimental cell or from small misalignments of the interferometer. To compensate them, powerful correction techniques can be applied and are given in more detail in Section 4.2 [22]. An example of a quantitative phase-contrast image obtained, of an alga *Pediastrum* sp. at high magnification ( $\times 100$ ), is shown in **Figure 2b**.

The fluorescence is implemented in the epifluorescence configuration, in such a way that the same sample is sequentially imaged by DHM and fluorescence modes on the same camera sensor. Applications of the combination of the DHM and fluorescence modes are given in Section 4.1.

In some applications, the color information is relevant. However, the configuration of **Figure 2a** is complex to adapt to several optical sources of different wavelengths. Indeed, in this case, the slant between the object and reference beams is identical for all the wavelengths, giving rise to fringe patterns with different inter-fringe spaces. This would make more difficult the processing with the Fourier method. In order to counter this limitation, we developed the color DHM instrument shown in **Figure 3** [23].

This color DHM is also based on a Mach-Zehnder configuration in which we added two afocal systems, L2-L3 and L4-L5, in the object and reference channels, respectively, between the microscope lenses and the lens in front of the camera sensor. In the object channel, a neutral density filter is placed in the back focal plane of L2. In the reference channel, a Ronchi grating is placed in the back focal plane of L4 and is



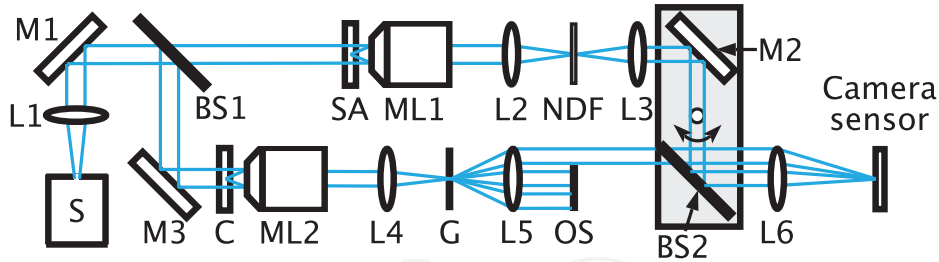


**Figure 3.** Color off-axis DHM configuration. S: optical source, L1-L6: lenses, ML1-ML2: microscope lenses, BS1-BS2: beam splitters, M1-M3: mirrors, SA: sample, C: optional compensation plate, NDF: neutral density filter, G: grating, and OS: optical stop.

imaged on the camera sensor by L5–L6. In the back focal plane of L5, an optical stop is placed to keep only one of the first diffraction orders. In this way to proceed, the slant between the object and reference beams on the camera sensor is changing with the wavelength, in such a way that the same spatial frequency of the fringes is kept on the sensor. Therefore, this configuration is operating for any wavelength in the visible range without having to adjust the fringe spacing to implement the Fourier method. In order to operate in the red (R), green (G), and blue (B) wavelengths, the partially spatially coherent illumination is created by the combination of three laser beams into the system using a ground glass as described hereinabove. It has to be emphasized that the grating also enables the use of reduced temporal coherence sources, such as LEDs [23]. Indeed, if a reduced temporal coherence source is used in the configuration of **Figure 2a**, the slant between the object and reference beams makes the fringe contrast not uniform over the field of view. We can even expect to have no fringe at all in some areas of the field of view. With the configuration of **Figure 3**, however, due to the properties of the diffraction by a grating, this issue is solved. This configuration indeed provides a uniform fringe contrast with reduced temporal coherence illumination, accordingly, the optical paths between the object and reference beams are finely equalized. This equalization is adjusted, thanks to the rotating mount on which the mirror M2 and the beam splitter BS2 are placed.

An example where the color DHM can provide relevant information is the routine analysis of clinical cervical samples for the prevention and the checking of the development of cancerous cells. Analyses are usually performed on classical ThinPrep slides with the Papanicolaou stain. In this way, we performed the analysis of samples with the color DHM and recorded multispectral holograms (**Figure 4a**). From the recorded hologram, we extracted the intensity and the phase images in three wavelengths separately: 639 nm (R), 532 nm (G), and 488 nm (B). The combination of the RGB intensity images of stained slides gives color intensity images comparable to those obtained with classical microscopy used by histopathologists (**Figure 4b**). In addition to this RGB intensity image, DHM gives, simultaneously on the same sample, quantitative phase-contrast imaging. In **Figure 4c**, it can be seen that typical dysplastic cells (big nucleus and small cytoplasm) have the highest optical thickness.

One of the targets with the DHM is the refocusing of objects that have been recorded out of focus. For that purpose, the implementation in Fourier optics, of the convolutional form of the free space propagation is used [24]. The complex amplitude distribution  $t_d$  reconstructed at a distance  $d$  along the optical axis, by computing the Kirchhoff–Fresnel propagation integral in the paraxial approximation, is expressed by:

$$t_d(x', y') = \exp(jkd) F_{x', y'}^{-1} \exp\left(-j\pi\lambda d \left(\nu_x^2 + \nu_y^2\right)\right) F_{\nu_x, \nu_y}^{+1} t_0(x, y) \quad (3)$$

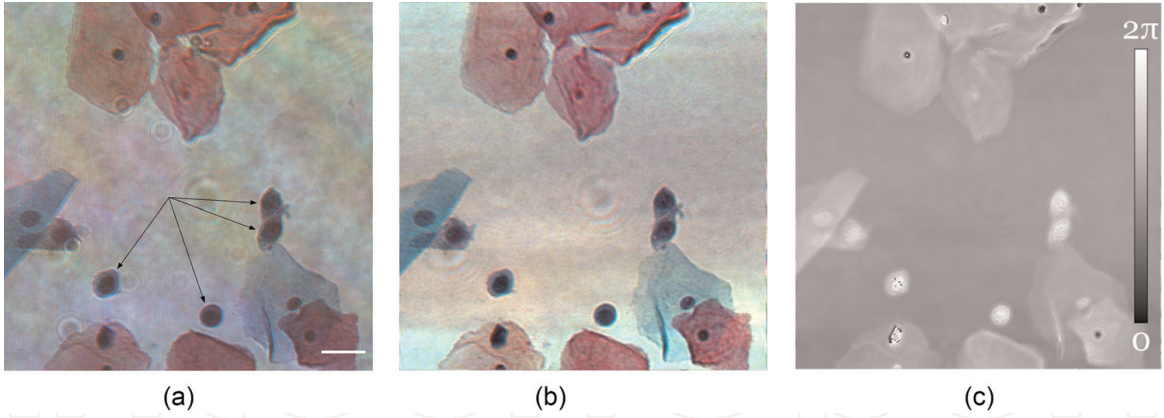


**Figure 4.** Images obtained with the color DHM of a clinical cervical sample. (a) color hologram image, (b) color intensity image, and (c) phase image in the red wavelength ( $R$ ). The arrows indicate typical dysplastic cells. Scale bar =  $20 \mu\text{m}$ .

where  $t_0$  is the complex amplitude of the optical field in the recorded plane,  $k = 2\pi/\lambda$  is the wavenumber,  $(x, y)$  and  $(x', y')$  are the spatial variables in the focus plane and in the reconstructed plane, respectively,  $(\nu_x, \nu_y)$  are the spatial frequencies,  $j = \sqrt{-1}$  and  $F^{\pm 1}$  denote the direct and inverse two-dimensional continuous Fourier transformations. In its discrete form with a sampling distance  $\Delta$ , Eq. (3) becomes:

$$t_d(s'\Delta, t'\Delta) = \exp(jkd)F_{s',t'}^{-1} \exp\left(\frac{-j\pi\lambda d}{N^2\Delta^2}(U^2 + V^2)\right)F_{U,V}^{+1}t_0(s\Delta, t\Delta) \quad (4)$$

where  $N$  is the number of pixels along the  $x$  and  $y$  directions;  $s, t, s', t', U,$  and  $V$  are integer numbers varying from 0 to  $N - 1$ , and  $F^{\pm 1}$  are here the direct and inverse discrete Fourier transformations.

The phase  $\varphi_{t_d}$  corresponding to the complex amplitude  $t_d$  is obtained by computing

$$\varphi_{t_d}(s'\Delta, t'\Delta) = \text{Arctan}_{2\pi}(\text{Im}[t_d(s'\Delta, t'\Delta)], \text{Re}[t_d(s'\Delta, t'\Delta)]) \quad (5)$$

where  $\text{Arctan}_{2\pi}$  is the two-parameters arctangent function, and  $\text{Im}[z]$  and  $\text{Re}[z]$  denote the imaginary and real parts of  $z$ , respectively.

This holographic reconstruction does not indicate for which distance  $d$  the best focus of an object is reached. In order to dispose of criteria giving the best plane of each object present in the field of view, we use several methods based on the conservation of the amplitude integration [25–27] or the invariance of the modulus of the Fourier transform during the propagation [28].

### 3. Noise reduction by the use of partially coherent illumination

To study the illumination by a partially spatially coherent illumination, the left image of **Figure 1** may be considered. In this configuration, the illumination is performed by the set of mutually incoherent point sources located within the aperture. As the locations of those points are different, each of them gives rise, after the collimation lens, to plane waves with different propagation angles. Therefore, each object is illuminated by a set of mutually incoherent plane waves having different propagation directions. For an unfocused object, it results that the propagation up to

the input focus plane of lens ML3 (in **Figure 2**) gives rise to a set of mutually incoherent diffraction patterns that are specifically shifted, due to the different propagation directions. Those shifts increase with the defocus distance  $d$ . It results that the digital holographic reconstruction creates a set of refocused objects at different locations in the reconstruction plane. This phenomenon results in a convolutional process [20], for an object defocused by a distance  $d$ , the complex amplitude  $\hat{t}_d(\mathbf{x})$ , extracted from the hologram in case of partial spatial coherence, is given by:

$$\hat{t}_d(\mathbf{x}) = A \iint d\mathbf{x}' p\left(\frac{2f(\mathbf{x} - \mathbf{x}')}{dD}\right) t_d(\mathbf{x}') \quad (6)$$

where  $\mathbf{x} = (x, y)$ ,  $A$  is a constant,  $p$  is the normalized pupil function equal to 1 within a circle of radius 1 and equal to zero outside,  $f$  is the focal length of the collimation lens,  $D$  is the diameter of the aperture in **Figure 1**, and  $t_d(\mathbf{x}')$  is the complex amplitude that would have been obtained in case of fully coherent illumination.

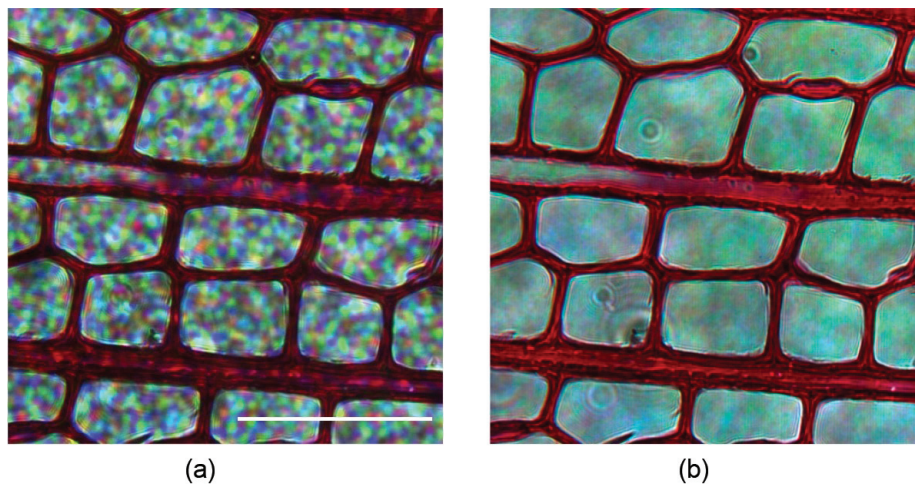


**Figure 5.** Color images obtained with the color DHM with a noise slide located at 1 mm. Laser sources, lens magnification  $\times 40$ , scale bar = 100  $\mu\text{m}$ , equivalent aperture size of (a) 1 mm, (b) 5 mm.

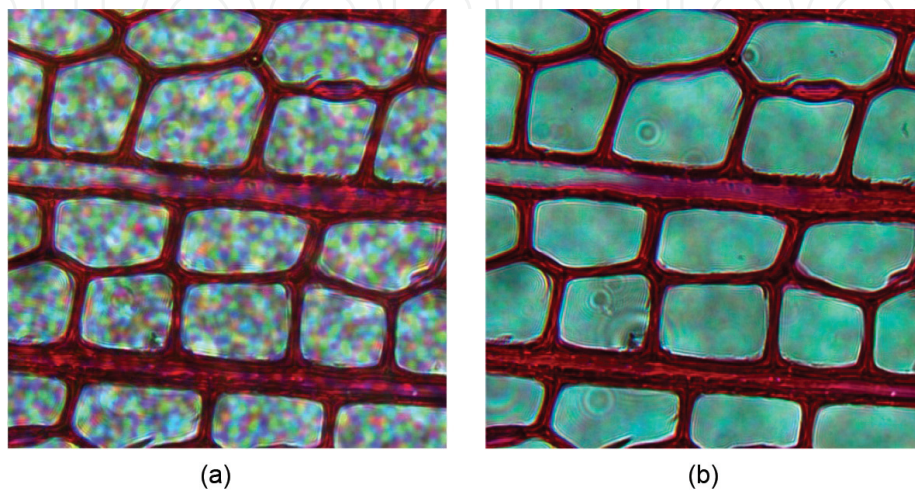


**Figure 6.** Color image obtained with the color DHM with a noise slide located at 1 mm. LED sources, lens magnification  $\times 40$ , (a) aperture size 1 mm, (b) aperture size 5 mm.



It results in an increasing loss of resolution when the defocus distance increases. The way to manage it consists to adjust the partial coherence by adapting  $D$  (left diagram in **Figure 1**) or the focusing distance of the laser beam with respect to the ground glass (right diagram in **Figure 1**), in such a way that the resolution requirement is filled for the longest defocus distance possible. The advantage of this phenomenon is the removal, by the convolution, of the defects of the experimental cell and of the optical system. Therefore, it is possible to implement a drastic reduction of the noise that happens with a fully coherent system. This noise reduction has been modeled and measured [29]. Examples of noise reduction obtained in color DHM are shown in **Figures 5** and **6**. The wood slice was placed in the color DHM configuration, and a contaminated slice with particles was placed at 1 mm of the wood slice. We recorded the pictures with the apertures of 1 mm and 5 mm with the LED illumination, or equivalently with the laser illumination. The focal length of L1 in **Figure 3** is  $f = 200$  mm. Experiments were performed with laser and LED sources.

The comparison of the results in **Figures 5** and **6** shows that the reduction of the spatial coherence has a major impact on the reduction of the noise created by out-of-focus disturbances. It is also to be noted that the reduction of the temporal coherence by replacing the lasers with LEDs (coherence length of 30 nm) gives, in this example, a weak reduction of the noise. This is due to the fact that the considered DHM configuration is in transmission and the noise-generating slide is relatively thin.

## 4. Applications

### 4.1 Multimodal DHM

The fluorescence mode in microscopy is of central importance in biology and biomedical applications, as specific fluorescent labeling allows us to tag specific structures and molecules in cells, tissues, and to perform cell analysis.

We were pioneers in the development of a multimodal DHM to combine the quantitative phase-contrast images provided by the recorded holograms and the fluorescence images of samples, labeled with fluorophores or that present an autofluorescence [19, 30, 31].

The quantitative phase-contrast imaging provides morphology and structural information on the sample. Fluorescence imaging provides information on molecules, thanks to the use of specific fluorophores. Therefore, the combination of both quantitative phase-contrast imaging and fluorescence imaging is of great interest, in particular in biomedical applications and cell biology. For that reason, this combination was afterward also performed by several authors [9, 32, 33].

One of the configurations we developed is presented in **Figure 2a**. In this setup, the fluorescence mode is obtained in reflection as in classical microscopy (epifluorescence mode), with the use of a classical fluorescence filter set selected for the fluorophore(s) to be studied. This filter set is inserted just below the microscope objective ML3 in the sample path (**Figure 2a**). A specific light source (LED) for microscope fluorescence mode is implemented for the excitation of the fluorophore(s) or the autofluorescence. The holograms and the fluorescence images are recorded with the same camera in a sequential mode. As the hologram is recorded in one shot, it allows to record the fluorescence signals with a very short delay.

The multimodal DHM working with partially coherent illumination allows to directly obtain the optical phase of the sample, the bright field image with reduced

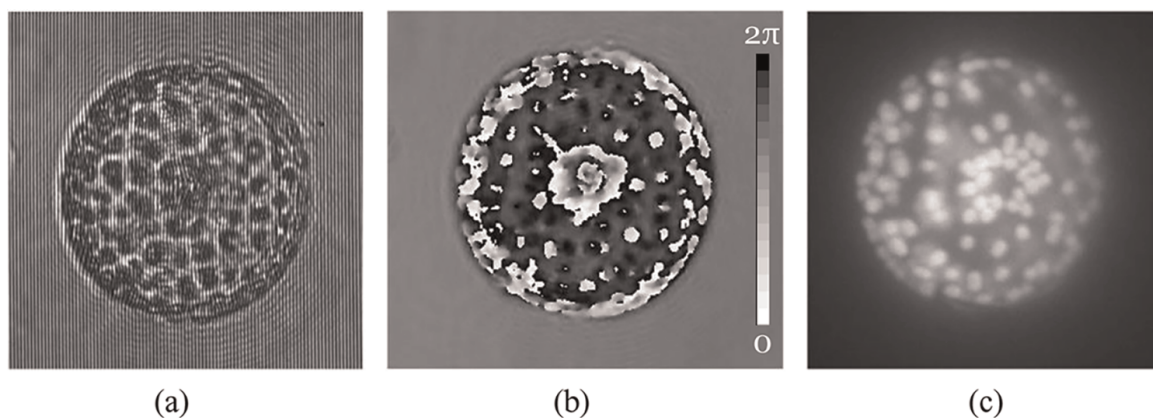


**Figure 7.** Images of a phytoplankton organism obtained with the multimodal DHM. (a) the hologram, (b) the phase image, and (c) the chlorophyll auto-fluorescence. These species form colonies and the fluorescence images show the individual cell chloroplast.

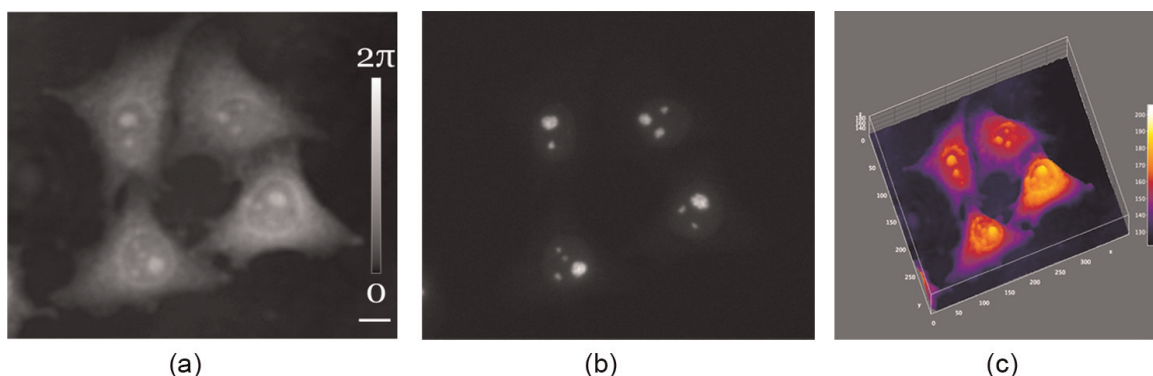


**Figure 8.** Validation of the visualization of nucleoli inside the nucleus of HeLa cells, in the phase image. These HeLa cells have one nucleolar protein labeled with the green fluorescent protein (GFP). (a) the phase image, (b) the GFP fluorescent image, (c) the 3D-plot of the phase image (a), unit as gray levels in (a). Scale bar = 10  $\mu\text{m}$ .

noise, and the fluorescence image. The combination of those images allows us to analyze the specimen in detail and brings precious information. An example obtained on a phytoplankton organism is presented in **Figure 7**.

Thanks to the overlay of the quantitative phase-contrast images and the fluorescent images, this DHM is a powerful tool to perform correlative quantitative phase-contrast-fluorescence microscopy. An example is presented in **Figure 8**, which shows the validation of the visualization of nucleoli inside the nucleus of HeLa cells in the phase image. The nucleoli are clearly visible on the phase image with their highest optical height. It is, therefore, possible to study the nucleoli thanks to the phase information, without fluorescence and in a noninvasive way.

Moreover, the recording of the quantitative phase information with low noise also enables the emulation of other classical microscopy modes. In particular, we emulated the differential interference contrast (DIC) mode, a classical tool to observe living cells [34].

#### 4.2 In-flow analysis using DHM

The DHM configurations described in Section 2 are based on Mach–Zehnder off-axis interferometers. As explained above, this allows the one-shot acquisition of the

hologram, that is, the extraction of the complex amplitude of the optical field,  $t_0(\mathbf{x})$ , from one single recorded image. The complex amplitude measured in one plane can be then numerically propagated in depth, that is, computed in other planes along the optical axis, giving  $t_d(\mathbf{x})$ , as described by Eq. (3) in Section 2; this process is known as the digital holographic reconstruction. This feature is of high interest for the fine analysis of dynamic phenomena, especially if the sample is thicker than the classical depth of field. The described technology is, therefore, well suited for the high-throughput, in-flow observation of objects in thick samples.

We developed in-flow DHM in partially coherent illumination, with specific algorithms for processing the holograms, resulting in high-quality refocused images of the objects of interest, regarding both optical phase and intensity [4, 35]. We used it in many applications, mainly in the environmental field, as illustrated in **Figure 9**, and in the biomedical field, as shown in **Figure 10**. Monochromatic ([4], **Figure 10**) or color RGB DHM ([35], **Figure 9**) were used in the different studies. The illumination was partially coherent, either both spatially and temporally (**Figure 9**) or only spatially while keeping a high temporal coherence (**Figure 10**).

The DHM configurations are those described in Section 2 above and in [4, 35]. The microscope objectives are Leica, magnification  $40\times$ , and numerical aperture 0.6. A flow chamber is placed in the object arm of the interferometer (position SA in **Figure 3**). The objects of interest are biological cells: either algal cells in **Figure 9**, or red blood cells in **Figure 10**. The cells are present in suspension in the sample, which is pulled into the flow chamber in such a way that the cells appear in the field of view of the microscope. A sequence of holograms is recorded in order to analyze a large number of cells.

In interferometric DHM, the knowledge of the complex amplitude,  $t_0(\mathbf{x})$ , extracted from the measured hologram, allows to undertake a powerful compensation of the aberrations in the field of view [35, 36]. One way exists to divide it by a blank complex amplitude,  $b(\mathbf{x})$ , which is the image containing all—and only—the aberrations due to the defects in the optical paths [35]:

$$t_{0c}(\mathbf{x}) = \frac{t_0(\mathbf{x})}{b(\mathbf{x})} \quad (7)$$

where  $t_{0c}(\mathbf{x})$  is the corrected complex amplitude.

However, in the case of the in-flow imaging in DHM, the objects of interest are moving in the field of view, whereas the permanent defects and aberrations are static. As we showed in [4, 35], the blank image,  $b(\mathbf{x})$ , can then be computed, in a very

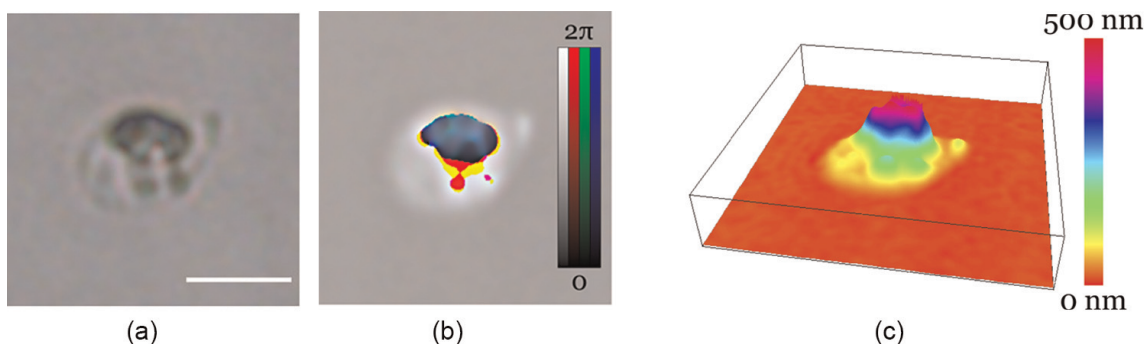


**Figure 9.** Microplankton organism analyzed using color in-flow DHM. Automatically corrected and refocused images of: (a) the amplitude modulus, (b) the optical phase, and (c) the corresponding optical thickness. Scale bar =  $10 \mu\text{m}$ .



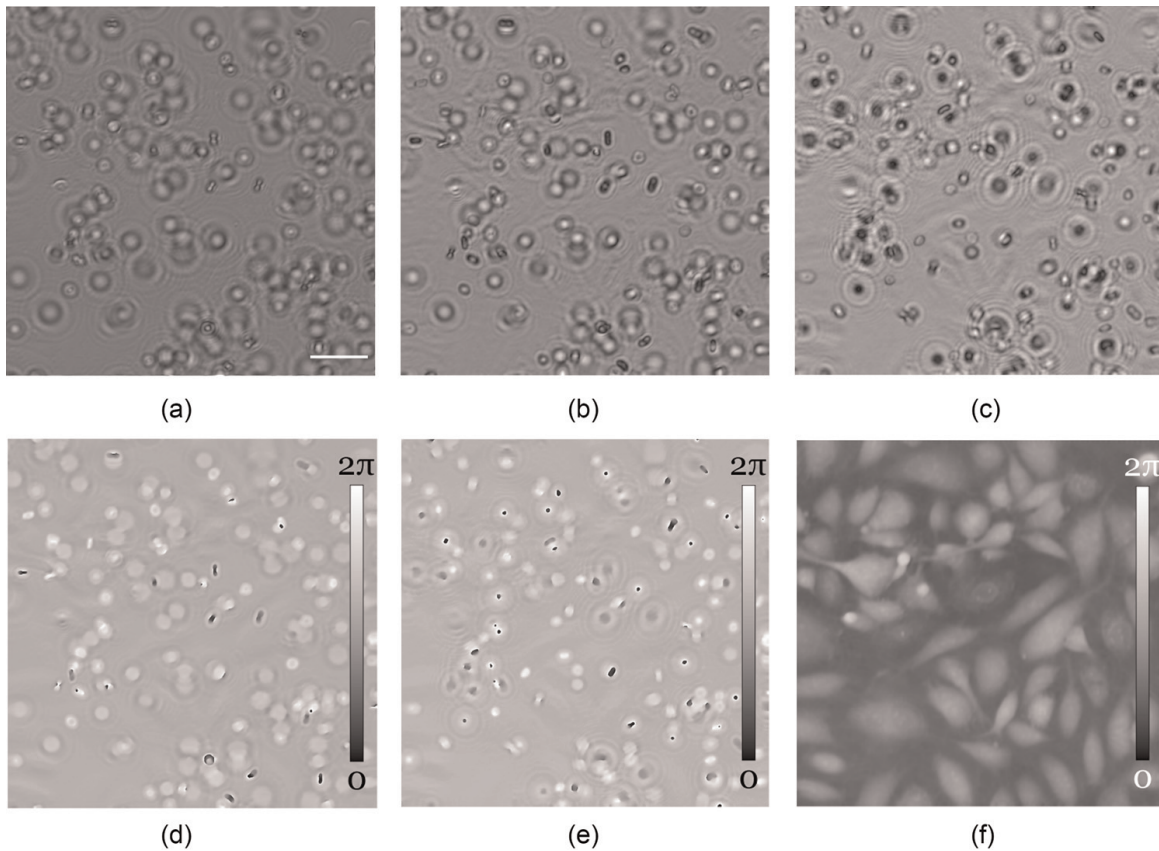


**Figure 10.** Red blood cells observed behind an endothelial cell layer using in-flow DHM. Amplitude moduli of corrected images of red blood cells: (a) in the recorded plane, (b) and (c) reconstructed in two different parallel planes, (d) and (e) phase images corresponding to (b) and (c), respectively, and (f) computed phase image of the endothelial cell layer. Different refocused red blood cells can be seen in (b)–(e). Scale bar = 20  $\mu\text{m}$ .

good approximation, as the averaged complex amplitude over all the images of the recorded sequence:

$$b(\mathbf{x}) = \frac{1}{N} \sum_{i=1}^N t_{0,i}(\mathbf{x}) \quad (8)$$

where  $t_{0,i}(\mathbf{x})$  is the complex amplitude extracted from the  $i$ -th hologram of the recorded sequence ( $i = 1, \dots, N$ ), and  $N$  is the number of recorded holograms in the sequence.

The blank,  $b(\mathbf{x})$ , is thus directly computed with the sequence of interest. It is not required to record a reference image separately. Two advantages result from this feature: (1) the blank well corresponds to the experiment itself, while a reference image recorded subsequently would be less close to the experimental conditions, and (2) the blank also contains the defects present on the walls of the flow chamber during the experiment.

The computation of the blank is efficient from about 100 averaged images. If the sequence experiment is very long, the blank  $b_i(\mathbf{x})$  for the  $i$ -th image  $t_{0,i}(\mathbf{x})$  can be computed with a moving average around this image:

$$b_i(\mathbf{x}) = \frac{1}{2P+1} \sum_{p=i-P}^{i+P} t_{0,p}(\mathbf{x}) \quad (9)$$



where  $2P + 1$  is the number of averaged images, and this equation does not work for the  $P$  first and the  $P$  last images of the sequence. This allows a powerful correction, by reducing the effects of the instabilities of the illumination.

Dividing every image of the sequence by the computed blank provides the automatic correction of the defects and aberrations, which are permanent in the field of view. For the color in-flow DHM, the described method also automatically corrects the color balance in the images as illustrated in **Figure 9**. The method is very powerful, giving efficiently corrected complex amplitudes, resulting in high-quality images of both the optical phase and intensity, for every image of the sequence.

Once the images are corrected, every object of interest is automatically refocused as explained in Section 2. This allows to observe each object present in the image, even if it was recorded out of its focal plane. The whole depth of the flow chamber is thus analyzed.

#### 4.2.1 An environmental application: the automatic analysis of plankton

We used the color in-flow DHM with LED illumination for the analysis of the microorganisms of plankton in pond and river water samples [35]. The algorithm described above was applied for the automatic correction of the permanent defects and aberrations, including the color balance, and for the automatic refocusing. **Figure 9** illustrates the study and shows an example of observed microorganisms.

#### 4.2.2 A biomedical application: the analysis of human red blood cells through a layer of endothelial cells

We also present here another interesting application of in-flow DHM with partially coherent illumination: the *in vitro* observation of red blood cells inside a flow chamber, whose wall was plated by endothelial cells. This endothelial cell layer allows to mimic the real blood vessels. Observing the behavior of red blood cells close to this layer is therefore essential from a biomedical point of view. We used here the laser source with the rotating ground glass. The correction method described above, in Eqs. (7)–(9), is particularly efficient for such a study. Indeed, with this method, the computed blank gives an image of the endothelial cell layer, which remains static in the field of view, whereas the images of the red blood cells, pulled in the flow chamber, are rid of the modulations due to this layer. Results are shown in **Figure 10**.

### 4.3 Other blood applications

DHM is well suited for the analysis of blood cells, especially human blood cells [6, 37, 38]. Firstly, the quantitative phase analysis yields a powerful measurement tool for the accurate characterization of blood cells. The phase is indeed related to the optical thickness of the cells. Secondly, the holographic reconstruction in depth allows the extension of the depth of investigation, in comparison with the usual depth of field in classical optical microscopy. This allows to study the motion of blood cells in thick samples, of the same order of magnitude as real human blood vessels. Thirdly, the knowledge of both the quantitative phase and intensity makes easier the automatic processing of a large number of images. Therefore, statistically significant samples can be efficiently studied.

In addition to the in-flow analysis described in 4.2.2, we present here two other applications we performed, illustrating the potential of DHM in blood cell analysis.

#### 4.3.1 Distribution of size and shape of red blood cells within one individual

All the red blood cells within one individual are not identical. Their size and shape are distributed over some range. Studying this distribution is important in biomedical research since it impacts platelet diffusion in blood flows. We used DHM for characterizing this distribution.

An example is shown in **Figure 11**, for one healthy individual (male, 27 years old). Microscope lenses Olympus, magnification  $63\times$ , and numerical aperture 0.7 were used. The illumination was made by a green laser source (532 nm) with rotating ground glass. The blood sample was diluted  $2000\times$  in the plasma of the donor, in order to avoid any osmotic shock, which would have resulted in a change in the shape and size of the red blood cells. Diluted blood is pulled into a flow chamber, before two-hour sedimentation. A sequence of holograms is then recorded by scanning the flow chamber. Holograms are processed using the method described in Section 4.2 for the compensation of defects and aberrations, and then refocusing. Biconcave red blood cells are then detected and segmented in each image using a method developed in [6], based on the normalized correlation product, denoted  $\tilde{\otimes}_{\Gamma}$ , which is defined by:

$$(g \tilde{\otimes}_{\Gamma} h)(\mathbf{x}) = \frac{|(g \otimes h)(\mathbf{x})|}{\|h\| \|g\|_{\Gamma}(\mathbf{x})} \quad (10)$$

where  $g(\mathbf{x})$  is the image containing the red blood cells to be detected,  $h(\mathbf{x})$  is a reference image containing a typical red blood cell in its center,  $|z|$  denotes the modulus of  $z$ ,  $\otimes$  is the usual correlation product,  $\|h\|$  is the Euclidean norm of  $h$ , computed by

$$\|h\| = \sqrt{(h \otimes h)(\mathbf{0})} \quad (11)$$

with  $\mathbf{0}$  being the zero vector, and  $\|g\|_{\Gamma}(\mathbf{x})$  is the moving norm of  $g$  over a domain  $\Gamma$ , which surrounds the red blood cell in  $h$  but centered in  $\mathbf{x}$ , and is given by:

$$\|g\|_{\Gamma}(\mathbf{x}) = \sqrt{(g^2 \otimes \gamma)(\mathbf{x})} \quad (12)$$

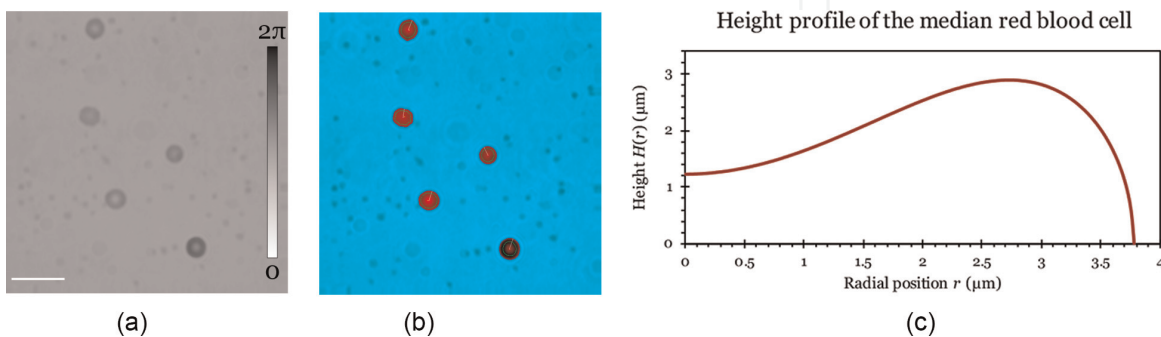


**Figure 11.**

Measurement of the statistical distribution of size and shape of the red blood cells within one individual.

(a) optical phase of an image in the recorded sequence, (b) same image with the automatically detected, segmented, and measured red blood cells, and (c) red blood cell shape corresponding to the median of the red blood cell distribution in the individual (568 red blood cells analyzed). Scale bar =  $20 \mu\text{m}$ .

with  $\gamma(\mathbf{x}) = 1$  inside  $\Gamma$  and  $\gamma(\mathbf{x}) = 0$  elsewhere. In practice, these expressions may be fast computed in the Fourier domain.

The normalized correlation product ranges from 0 to 1, exhibiting local maxima, close to 1, when a red blood cell is detected. Therefore, a fixed threshold applied to the image of the normalized correlation product allows to identify the position of each red blood cell. The segmentation is operated by applying a threshold to the phase image. Four parameters are then measured in each detected red blood cell: the mean radius, the minimal phase in the central part, the mean radius of the crest, and the mean phase value on the crest. From these four parameters, the parameters  $R$ ,  $\alpha$ ,  $\beta$ , and  $\delta$  in the following equation are assessed, commonly used for characterizing the height profile  $H(r)$  of red blood cells in numerical simulations:

$$H(r) = 2R\sqrt{1 - \frac{r^2}{R^2}} \left[ \alpha + \beta \frac{r^2}{R^2} + \delta \frac{r^4}{R^4} \right] \quad (13)$$

with  $r$  the radial position with respect to the center of the red blood cell. Results are given in **Figure 11**.

#### 4.3.2 Statistical analysis of spread platelets from healthy and dialyzed donors

We also used DHM for an accurate analysis of the spreading of platelets, while comparing healthy volunteers and dialyzed patients [6]. Results are illustrated in **Figure 12**. The spreading occurred in glass slides surmounted by wells. For each of the 14 individuals of the study, seven healthy and seven dialyzed, six wells were used: two coated with laminin, two coated with collagen IV, and two without any coating, denoted as control. Platelet-rich plasma from each individual was poured into each well. Subsequent sedimentation allows the platelets to spread onto the slide, before washing and fixation. Using this experimental procedure, with the sedimentation step for the spreading of platelets, enhances the reproducibility. Each well was then analyzed using a color DHM working in partially spatially coherent illumination, made by three laser sources followed by a rotating ground glass. Forty holograms were recorded for each well. The processing of holograms, including the compensation of

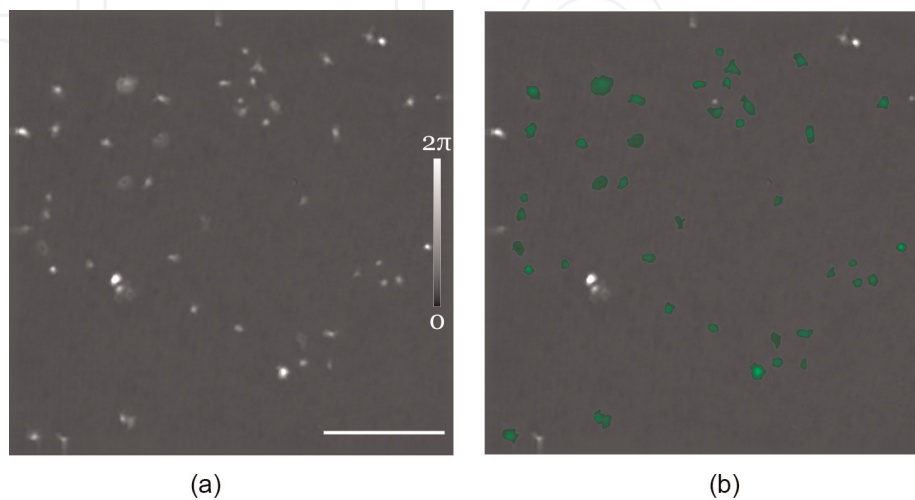


**Figure 12.**

*Analysis of the platelet spreading using DHM, with the comparison between healthy and dialyzed donors. (a) example of a phase image obtained, and (b) the same image with the automatically detected and segmented single platelets, with the automatic rejection of platelets at the borders and platelets forming aggregates. Scale bar 50  $\mu\text{m}$ .*

aberrations, the refocusing, the detection, and the segmentation of platelets, was performed as described in 4.2 and 4.3.1. For every detected platelet, several parameters were measured, whose surface area  $S$ , optical volume  $V$ , and average optical height  $\hat{h}$ .

Whereas the surface area  $S$  covered by each platelet can also be measured in classical microscopy, the measurement of the average optical height  $\hat{h}$ , which provides information about the efficiency of the platelet spreading, is a huge advantage of DHM in this study. We hence performed a statistical analysis of the three-dimensional morphology of single spread platelets in both healthy volunteers and dialyzed patients, and demonstrated, for the first time to our knowledge, a significant difference between both.

## 5. Conclusions

In this chapter, we have described the advantages of digital holographic microscopy (DHM) working with partially coherent illumination. This illumination drastically reduces the speckle noise that alters the images in both the amplitude modulus and the phase images. This opens the investigation of numerous applications with instruments that are robust and easy to use. The instrumentation is accompanied by software allowing the hologram processing in an automated way.

We have depicted several DHM configurations that we developed as a color DHM and a multimodal fluorescence DHM. We have presented different valuable applications that we implemented and that show the high-quality image obtained, which demonstrate the high capabilities of the technology in the biomedical and the environmental fields.

## Acknowledgements

The research was supported by the Walloon Region in the frame of the Decisiv and the HoloCancer projects and L'Institut d'encouragement de la Recherche scientifique et de l'Innovation de la Région de Bruxelles-Capitale (IRSIB-INNOVIRIS) in the frame of the HoloFlow Impulse project.

Dr. Jérôme Dohet-Eraly was Aspirant and then Chargé de Recherches du Fonds de la Recherche Scientifique – FNRS (F.R.S.-FNRS, Belgium).

## Conflict of interest

The authors declare no conflict of interest.



IntechOpen

### **Author details**

Frank Dubois<sup>1\*</sup>, Catherine Yourassowsky<sup>1</sup>, Karim Zouaoui Boudjeltia<sup>2</sup> and Jérôme Dohet-Eraly<sup>1</sup>


1 Université libre de Bruxelles – Chimie physique, Microgravity Research Centre, Bruxelles, Belgium

2 Université libre de Bruxelles – Laboratoire de Médecine expérimentale, Charleroi, Belgium

\*Address all correspondence to: frank.dubois@ulb.be

### **IntechOpen**

---

© 2022 The Author(s). Licensee IntechOpen. This chapter is distributed under the terms of the Creative Commons Attribution License (<http://creativecommons.org/licenses/by/3.0>), which permits unrestricted use, distribution, and reproduction in any medium, provided the original work is properly cited. 

## References

- [1] Schnars U, Jüptner WPO. Digital recording and numerical reconstruction of holograms. *Measurement Science and Technology*. 2002;**13**:R85-R101. DOI: 10.1088/0957-0233/13/9/201
- [2] Dubois F, Joannes L, Legros JC. Improved three-dimensional imaging with a digital holography microscope with a source of partial spatial coherence. *Applied Optics*. 1999;**38**: 7085-7094. DOI: 10.1364/AO.38.007085
- [3] Marquet P, Rappaz B, Magistretti PJ, Cuche E, Emery Y, Colomb T, et al. Digital holographic microscopy: a noninvasive contrast imaging technique allowing quantitative visualization of living cells with subwavelength axial accuracy. *Optics Letters*. 2005;**30**: 468-470. DOI: 10.1364/OL.30.000468
- [4] Yourassowsky C, Dubois F. High throughput holographic imaging-in-flow for the analysis of a wide plankton size range. *Optics Express*. 2014;**22**: 6661-6673. DOI: 10.1364/OE.22.006661
- [5] O'Connor T, Shen J-B, Liang BT, Javidi B. Digital holographic deep learning of red blood cells for field-portable, rapid COVID-19 screening. *Optics Letters*. 2021;**46**:2344-2348. DOI: 10.1364/OL.426152
- [6] Dohet-Eraly J, Zouaoui Boudjeltia K, Rousseau A, Queeckers P, Lelubre C, Desmet JM, et al. Three-dimensional analysis of blood platelet spreading using digital holographic microscopy: a statistical study of the differential effect of coatings in healthy volunteers and dialyzed patients. *Biomedical Optics Express*. 2022;**13**: 502-513. DOI: 10.1364/BOE.448817
- [7] Zhang T, Yamaguchi I. Three-dimensional microscopy with phase-shifting digital holography. *Optics Letters*. 1998;**23**:1221-1223. DOI: 10.1364/OL.23.001221
- [8] Cuche E, Bevilacqua F, Depeursinge C. Digital holography for quantitative phase-contrast imaging. *Optics Letters*. 1999;**24**:291-293. DOI: 10.1364/OL.24.000291
- [9] Park Y, Popescu G, Badizadegan K, Dasari RR, Feld MS. Diffraction phase and fluorescence microscopy. *Optics Express*. 2006;**14**:8263-8268. DOI: 10.1364/OE.14.008263
- [10] Barty A, Nugent KA, Paganin D, Roberts A. Quantitative optical phase microscopy. *Optics Letters*. 1998;**23**: 817-819. DOI: 10.1364/OL.23.000817
- [11] Luo W, Zhang Y, Feizi A, Göröcs Z, Ozcan A. Pixel super-resolution using wavelength scanning scanning. *Light: Science and Applications*. 2016;**5**: e16060. DOI: 10.1038/lsa.2016.60
- [12] Tian L, Liu Z, Yeh L-H, Chen M, Zhong J, Waller L. Computational illumination for high-speed *in vitro* Fourier ptychographic microscopy. *Optica*. 2015;**2**:904-911. DOI: 10.1364/OPTICA.2.000904
- [13] Podgorski T, Callens N, Minetti C, Coupier G, Dubois F, Misbah C. Dynamics of vesicle suspensions in shear flow between walls. *Microgravity Science and Technology*. 2011;**23**:263-270. DOI: 10.1007/s12217-010-9212-y
- [14] Callens N, Minetti C, Coupier G, Mader M-A, Dubois F, Misbah C, et al. Hydrodynamic lift of vesicles under shear flow in microgravity. *Europhysics Letters*. 2008;**83**:24002. DOI: 10.1209/0295-5075/83/24002
- [15] Zegers I, Carotenuto L, Evrard C, Garcia-Ruiz J, De Gieter P, Gonzales-

- Ramires L, et al. Counterdiffusion protein crystallisation in microgravity and its observation with PromISS (protein microscope for the international space station). *Microgravity Science and Technology*. 2006;**18**:165-169. DOI: 10.1007/BF02870402
- [16] Schilling BW, Poon T-C, Indebetouw G, Storrie B, Shinoda K, Suzuki Y, et al. Three-dimensional holographic fluorescence microscopy. *Optics Letters*. 1997;**22**:1506-1508. DOI: 10.1364/OL.22.001506
- [17] Rosen J, Brooker G. Digital spatially incoherent fresnel holography. *Optics Letters*. 2007;**32**:912-914. DOI: 10.1364/OL.32.000912
- [18] Rosen J, Brooker G. Non-scanning motionless fluorescence three-dimensional holographic microscopy. *Nature Photonics*. 2008;**2**:190-195. DOI: 10.1038/nphoton.2007.300
- [19] Dubois F, Yourassowsky C. Method and device for obtaining a sample with three-dimensional microscopy. Patents. EP 01870147 (2001), EP1399730 B1, US 7009700 B2 (2006)
- [20] Dubois F, Requena ML, Minetti C, Monnom O, Istasse E. Partial spatial coherence effects in digital holographic microscopy with a laser source. *Applied Optics*. 2004;**43**:1131-1139. DOI: 10.1364/AO.43.001131
- [21] Kreis T. Digital holographic interference-phase measurement using the Fourier-transform method. *Journal of the Optical Society of America. A*. 1986;**3**:847-855. DOI: 10.1364/JOSAA.3.000847
- [22] Zouaoui Boudjeltia K, Ribeiro de Sousa D, Uzureau P, Yourassowsky C, Perez-Morga D, Courbebaisse G, et al. Quantitative analysis of platelets aggregates in 3D by digital holographic microscopy. *Biomedical Optics Express*. 2015;**6**:3556-3563. DOI: 10.1364/BOE.6.003556
- [23] Dubois F, Yourassowsky C. Full off-axis red-green-blue digital holographic microscope with LED illumination. *Optics Letters*. 2012;**37**:2190-2192. DOI: 10.1364/OL.37.002190
- [24] Nazarathy M, Shamir J. Fourier optics described by operator algebra. *Journal of the Optical Society of America*. 1980;**70**:150-159. DOI: 10.1364/JOSA.70.000150
- [25] Dubois F, Schockaert C, Callens N, Yourassowsky C. Focus plane detection criteria in digital holography microscopy by amplitude analysis. *Optics Express*. 2006;**14**:5895-5908. DOI: 10.1364/OE.14.005895
- [26] Dohet-Eraly J, Yourassowsky C, Dubois F. Refocusing based on amplitude analysis in color digital holographic microscopy. *Optics Letters*. 2014;**39**:1109-1112. DOI: 10.1364/OL.39.001109
- [27] Dubois F, El Mallahi A, Dohet-Eraly J, Yourassowsky C. Refocus criterion for both phase and amplitude objects in digital holographic microscopy. *Optics Letters*. 2014;**39**:4286-4289. DOI: 10.1364/OL.39.004286
- [28] Dohet-Eraly J, Yourassowsky C, Dubois F. Fast numerical autofocus of multispectral complex fields in digital holographic microscopy with a criterion based on the phase in the Fourier domain. *Optics Letters*. 2016;**41**:4071-4074. DOI: 10.1364/OL.41.004071
- [29] Dohet-Eraly J, Yourassowsky C, El Mallahi A, Dubois F. Quantitative assessment of noise reduction with partial spatial coherence illumination in

digital holographic microscopy. *Optics Letters*. 2016;**41**:111-114. DOI: 10.1364/OL.41.000111

[30] Dubois F, Yourassowsky C, and Monnom O. Microscopie en holographie digitale avec une source partiellement cohérente. In: Faupel M, Smigielski P, Grzymala R, editors. *Imagerie et Photonique pour les Sciences du Vivant et de la Médecine*. Fontis Media; 2004. p. 287-302

[31] Dubois F, Yourassowsky C, Callens N, Minetti C, Queeckers P, Podgorski T, et al. Digital holographic microscopy working with a partially spatial coherent source. In: Ferraro P, Wax A, Zalevsky Z, editors. *Coherent Light Microscopy, Imaging and Quantitative Phase Analysis*. Berlin: Springer; 2011. p. 31-59

[32] Quan X, Nitta K, Matoba O, Xia P, Awatsuji Y. Phase and fluorescence imaging by combination of digital holographic microscopy and fluorescence microscopy. *Optical Review*. 2015;**22**:349-353. DOI: 10.1007/s10043-015-0042-4

[33] Nygate YN, Singh G, Barnea I, Shaked NT. Simultaneous off-axis multiplexed holography and regular fluorescence microscopy of biological cells. *Optics Letters*. 2018;**43**:2587-2590. DOI: 10.1364/OL.43.002587

[34] Dubois F, Yourassowsky C, Monnom O, Legros JC, Debeir O, Van Ham P, et al. Digital holographic microscopy for the three-dimensional dynamic analysis of in vitro cancer cell migration. *Journal of Biomedical Optics*. 2006;**11**:054032. DOI: 10.1117/1.2357174

[35] Dohet-Eraly J, Yourassowsky C, Dubois F. Color imaging-in-flow by digital holographic microscopy with permanent defect and aberration

corrections. *Optics Letters*. 2014;**39**:6070-6073. DOI: 10.1364/OL.39.006070

[36] Colomb T, Cuche E, Charrière F, Kühn J, Aspert N, Montfort F, et al. Automatic procedure for aberration compensation in digital holographic microscopy and applications to specimen shape compensation. *Applied Optics*. 2006;**45**:851-863. DOI: 10.1364/AO.45.000851

[37] O'Connor T, Santaniello S, Javidi B. COVID-19 detection from red blood cells using highly comparative time-series analysis (HCTSA) in digital holographic microscopy. *Optics Express*. 2022;**30**:1723-1736. DOI: 10.1364/OE.442321

[38] Bianco V, Merola F, Miccio L, Memmolo P, Gennari O, Paturzo M, et al. Imaging adherent cells in the microfluidic channel hidden by flowing RBCs as occluding objects by a holographic method. *Lab on a Chip*. 2014;**14**:2499-2504. DOI: 10.1039/c4lc00290c